Muhammad A Imam and Ramana G Reddy*

# A Review of Boron-Rich Silicon Borides Based on Thermodynamic Stability and Transport Properties of High-Temperature Thermoelectric Materials

https://doi.org/10.1515/htmp-2018-0077
Received May 04, 2018; accepted September 14, 2018

**Abstract**: In this study, the performance of a boron-rich Si-B system containing ~ 2–25 mol% Si is reviewed as a high-temperature thermoelectric material. In this review, both thermodynamic stability and transport properties are evaluated to understand the high-temperature thermoelectric performance of the Si-B system. The thermodynamic properties, such as Gibbs energy and activity coefficient, of the Si-B system were calculated and compared to the literature data. Thermoelectric properties such as Seebeck coefficient, electrical conductivity, and thermal conductivity were reviewed for the Si-B system. It is found that the composition and processing techniques are critical for obtaining higher thermoelectrical properties and thus also true for the figure of merit ZT. The entropy (degree of randomness) of a system has a remarkable effect on ZT. The highest ZT obtained for this system is approximately 0.2 at 90% B ($SiB_6$ + $SiB_n$) containing $SiB_n$ phase, shows the lowest entropy (~32 J/mol*K) in this system at 1100 K.

**Keywords**: Silicon-Boron phase diagram, thermoelectric materials, thermodynamic properties, figure of merit (ZT)

## Introduction

Industrial civilization relies heavily on energy consumption in various forms. According to the U.S. Energy Information Administration (EIA), the annual global energy consumption in 2012 was 524 quadrillions Btu, which is equivalent to 150 trillion KWh [1]. The world's overall energy consumption demand is increasing every day. Alternate sources of energy, such as solar energy, wind power and ocean wave energy, have already been exploited to a good extent to meet an ever-increasing demand for world-wide energy consumption. Some of these sources are currently used in various systems, either in the experimental stage or the industrial production. Fossil fuels are the primary source of energy. Fossil fuels are burnt to generate heat and also to produce energy. This causes the greenhouse effect and the consequent catastrophic climate change. On the other hand, heat is also generated from many other mechanical and electrical systems during the industrial operation. In addition, all automotive systems generate an enormous amount of heat. Some of our household work also requires medium to quite high temperatures, such as the use of kitchen equipment. The heat from these sources can be utilized as renewable sources of energy, which can prevent further worsening of climate due to the greenhouse effect by reducing the demand for fossil fuels.

Industrial waste heat is not measured precisely. However, several studies have anticipated that about 20–50% of industrial energy consumption is eventually left as waste heat. This waste heat can be utilized through several recovery techniques such as the use of a regenerator, recuperator, waste heat boiler, or thermoelectric generator [2]. Most of the industrial processes need high-temperature thermoelectric generators, whereas most of the efficient thermoelectric generators are operated at lower temperature [3]. The better utilization of industrial waste heat requires a high-temperature thermoelectric generator.

Thermoelectric materials generate electricity by converting the temperature difference of the system into current. The heat difference can be utilized through the application of proper materials to generate the electricity. Thermoelectric materials can also be employed for transforming waste or additional heat generated by many sources such as solar radiation, industrial processes, automotive systems, and household appliances to produce electricity [4, 5]. A typical thermoelectric device is made of solid state materials. This process of generating electricity overcomes the shortcomings of the conventional electricity generator in many ways, including the use of non-moving parts, and being silent, reliable, scalable and, ideal for small, distributed power generation [5].

***Corresponding author: Ramana G Reddy,** Department of Metallurgical and Materials Engineering, The University of Alabama, Tuscaloosa, AL 35487, USA, E-mail: rreddy@eng.ua.edu
**Muhammad A Imam,** Department of Metallurgical and Materials Engineering, The University of Alabama, Tuscaloosa, AL 35487, USA, E-mail: maimam@crimson.ua.edu

## Backgrounds of thermoelectric effect

Thomas Johann Seebeck first introduced the concept of thermoelectric effect in 1823 [6]. He studied the voltage difference across the conductor's hot and cold junctions. This phenomenon is known as Seebeck effect. The thermoelectric potential gradient (ΔV) generated in the circuit (Figure 1) between the cold (T) and the hot junction (T + ΔT). This thermoelectric potential is called Seebeck electromotive force. The thermoelectric potential gradient (ΔV) is directly proportional to the temperature gradient (ΔT) between the hot and the cold junction. The ratio of the thermoelectric potential gradient and temperature gradient is known as Seebeck coefficient (α) (eq. (1)) [4]

$$\alpha = \frac{\Delta V}{\Delta T} \tag{1}$$

The thermoelectric efficiency is measured by the dimensionless thermoelectric figure of merit (ZT). ZT depends on the material's Seebeck coefficient (α), electrical conductivity (σ) and thermal conductivity (κ) [7, 8] and is given by eq. (2).

$$ZT = \frac{\alpha^2 \sigma\ T}{k} \tag{2}$$

A high ZT value endorses a more efficient conversion of heat to electricity, with T being the absolute operating temperature of the thermoelectric device. The thermal conductivity of these material has three parts containing contributions from lattice vibration ($\kappa_l$), photons ($\kappa_p$) and electrons ($\kappa_e$) [9].

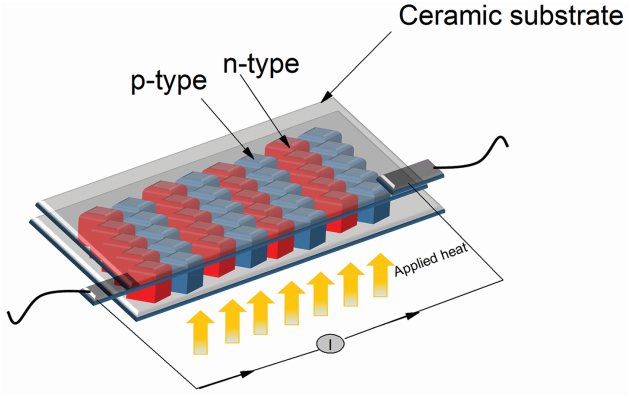


**Figure 1:** Illustration of seebeck effect.

At room temperature (300 K), the best thermoelectric materials are currently telluride-based materials, such as $Bi_2Te_3$(ZT ~ 1) and $Bi_2Te_3/Sb_2Te_3$ (ZT ~ 2.2) [8, 10]. In the mid-range temperature (400 K–800 K) region, several studies have found higher ZT existing in BiSbTe ($ZT_{max}$ ~ 1.5), PbTe ($ZT_{max}$ ~ 1.6), PbTeSe ($ZT_{max}$ ~ 1.7), and CoSb3 ($ZT_{max}$ ~ 1.6) [5, 11]. ZT increases with an increase in temperature for this temperature region [10]. After that, ZT decreases with the subsequent increase in temperature. These thermoelectric materials are not good candidates for a very high-temperature application because of the reduced value of ZT, as well as low thermal stability at the higher temperature. For high-temperature applications, GeSi ($ZT_{max(1123K)}$ ~ 2) is used for the generation of space power [5, 12, 13]. Although GeSi shows both higher ZT and higher thermal stability (stable up to 1573 K) at a high temperature, it also has a decreasing trend of ZT after 1123 K. Similar trend is also observed for the complex Zintl Phase $Yb_{14}SbMn_{11}$ ($ZT_{max}$ ~ 1) at 1200 K [5]. These materials are not efficient after a certain temperature level. This critical condition for high-temperature materials needs to be considered for prospective thermoelectric power generation.

In this review article, the boron-rich Si-B semiconductor system is discussed for high-temperature thermoelectric materials. It has a very high thermal stability (~1543–2293 K) depending on the molar ratio [14]. Moreover, the literature suggests an increasing trend of ZT up to 1273 K. All of the aforementioned criteria make Si-B system a feasible choice for high-temperature thermoelectric materials. A detailed discussion of thermodynamic stability and thermoelectric properties is presented here based on calculations and literature data.

## Thermodynamic stability of Si-B system

In the Si-B system, the boron-rich composition has drawn a wide attention among researchers in recent years due to its advantages for high-temperature thermoelectric materials [15]. Several studies have dealt with the thermodynamic properties of the Si-B system [16–22]. The thermodynamic stability of the boron-rich Si-B system is evaluated from the Si-B phase diagram and its thermodynamic properties, including activity and Gibbs energy calculation. The Si-B phase diagram, illustrated in Figure 2, is obtained from the thermodynamic modeling software Thermo-Cal [23]. In addition, experimental data indicates the presence of these three binary phases, namely $SiB_3$, $SiB_6$ and $SiB_n$

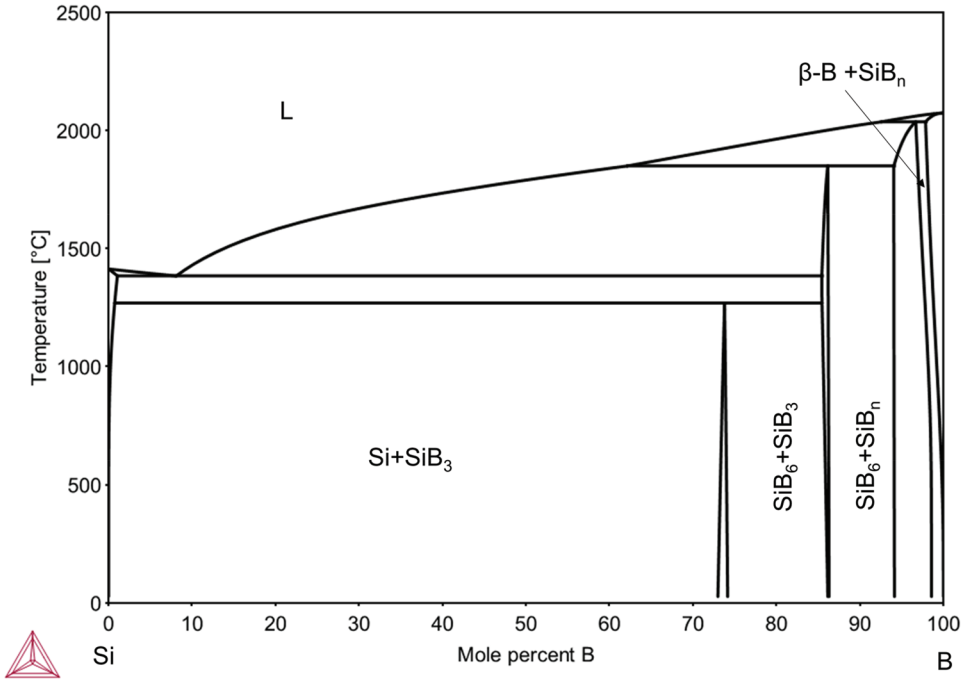


**Figure 2:** Si-B phase diagram [22].

**Table 1:** Boron-rich phases in the Si-B system.

| Phases | Composition (Mol. % Si) | | Stoichiometry |
|---|---|---|---|
| | Thermo-Cal [23] | Literature [14, 21] | |
| Silicon triboride | ~27–25 | ~21.5–26 | $SiB_3$ |
| Silicon hexaboride | ~13.7–13.85 | 14.2 | $SiB_6$ |
| Silicon n-boride | ~6–2 | ~6–2 | $SiB_n$ (n = 12–50) |

[24]. The main phases in the boron-rich Si-B systems are summarized in Table 1.

Although the composition is slightly different from that found in the literature, the calculated phase diagram shows a good consistency with the literature [14, 21]. Only the silicon hexaboride ($SiB_6$) phase shows a small difference in the phase diagram. In the literature [24], it shows only one single composition, whereas this calculation provides a small (~13.7–13.85 mol% Si) range of the composition for this phase. Thermodynamic properties of these three phases are reviewed here to determine their suitability for high-temperature thermoelectric applications.

## Silicon tri boride ($Sib_3$):

$SiB_3$ is one of the single binary phases found in the Si-B system. Although Moissan and Stokes mentioned $SiB_3$ phase in 1900 [25], they did not confirm the single phase. In 1955, it was first reported that $SiB_3$ single phase could be prepared from the elements by hot pressing at a temperature range of 1873–2073 K [26]. According to Thermo-Calc software modeling (Figures 2 and 3) and literature, the range of this single phase exists between 21 and 27 mol% of Si (Table 1). The invariant reaction for the $SiB_3$ phase can be found in Figure 2 at 1542 K. This invariant reaction (eq. (3)) for the rhombohedral α-$SiB_3$ phase is also reported in the literature [20, 24]. The alternative orthorhombic phase of β-$SiB_3$ is confirmed in another study [27]. A further compound named $SiB_4$ is also reported in several other studies [28–30]. $SiB_3$ has a wider homogeneity range ($SiB_{2.8-4.0}$) and it is closer to $SiB_3$ than $SiB_4$ [31].

$$\alpha Si + SiB_6 \leftrightarrow SiB_3 \ (peritectoid) \tag{3}$$

The change in Gibbs energy for this phase is summarized from different literatures in Table 2. In Figure 3, the change in Gibbs energy of $SiB_3$ at 1100 K was illustrated with increasing mol % of Si. This data is acquired from the thermodynamic modeling of Si-B system by using Thermo-Calc software. It can be inferred from the figure that the most favorable condition for this phase is ~ 27 mol % of Si in Si-B system. The lowest value for formation Gibbs energy ($\Delta G^o$) for this binary phase is calculated to be –27.28 KJ/mol at 1100 K from the current thermodynamic modeling, thus inferring from the current model that $SiB_3$ binary phase is

**Table 2:** Comparison of the thermodynamic properties of the Si-B system.

| Phases | $\Delta G_f^o$(KJ/mol) at 1800 K (*1757 K,**1100 K) | | | | | | |
|---|---|---|---|---|---|---|---|
| | [32] | [33] | [34] | [35] | [21]* | Current model [23] | |
| $SiB_3$ | – | −24.098 | −31.98 | −17.978 | | −56.87 | −27.28** |
| $SiB_6$ | −54 ± 15 | −46.310 | −66.619 | −40.659 | −68.6 ± 1.2 | −54.405 | −25.02** |
| $SiB_n$ | −108 ± 32.8 (n = 15) | −56.102 (n = 12) | – | −57.37 (n = 14) | −105.5 ± 3 | −51.20 | −22.69** |

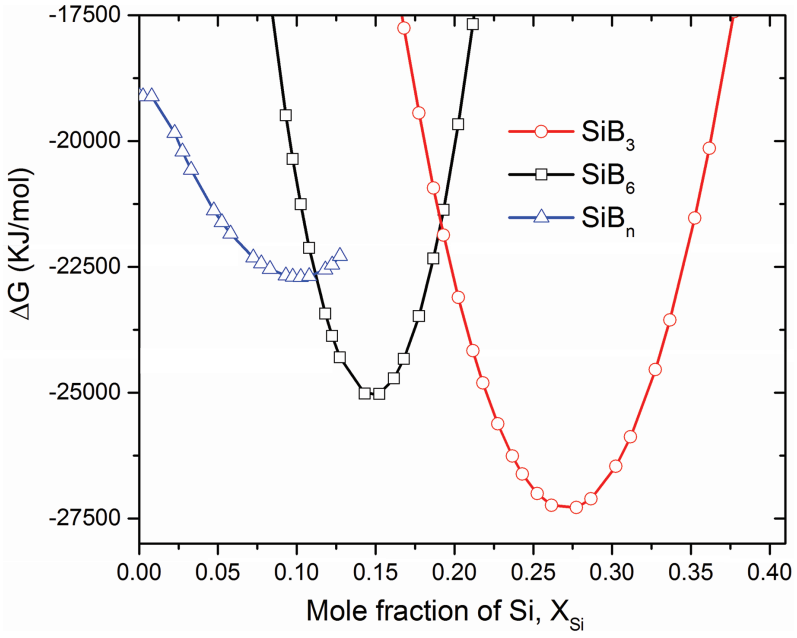


**Figure 3:** The change in Gibbs-free energy (ΔG) with the function of mol % of Si at 1100 K.

more stable than $SiB_6$. The formation Gibbs energy of this phase at 1800 K from different studies is also tabulated in Table 2. The activities of Si and B are also calculated by using Thermo-Calc (Figure 4). As seen in Figure 4, the range of activity for Si and B was found as ~ 0.53–0.99 and ~ 0.6–0.48 respectively in $SiB_3$ phase.

Furthermore, entropy is calculated to confirm the degree of randomness in this phase. Figure 5 provides the entropy change of the Si-B system at 1100 K. $SiB_3$ shows the highest entropy (34.9 J/mol*K) among these three phases.

## Silicon hexaboride ($Sib_6$)

Moissan and Stokes first introduced $SiB_6$ binary phase in 1900 [25]. They obtained a mixture of $SiB_6$ and $SiB_3$. Afterward, several studies were done to confirm the single phase of $SiB_6$ [36–39] but were not successful. Cline finally reported the single binary phase of $SiB_6$ in 1958–59 [40, 41]. The $SiB_6$ is considered as a line compound in the previous literature [24]. However, the current modeling by using Thermo-Calc shows a small range of composition at around ~ 13.7–14.28 mol% of Si (Figure 2). The invariant peritectic reaction (eq. (4)) for this phase is found at 2122 K, as shown in Figure 2, which is also consistent with the existing literature [20].

$$Liquid + SiB_n \leftrightarrow SiB_6 \ (Peritectic) \tag{4}$$

The lowest value of Gibbs energy for formation of this compound is found to be −25.02 kJ/mol at 1100 K for the same compositional range (Figure 3). This confirms the stability of the $SiB_6$ phase in this compositional range. Table 2 presents the Gibbs energy for this phase at 1800 K as found in different studies. In Figure 4, a sharp slope of activity for B and Si is observed for this phase region at

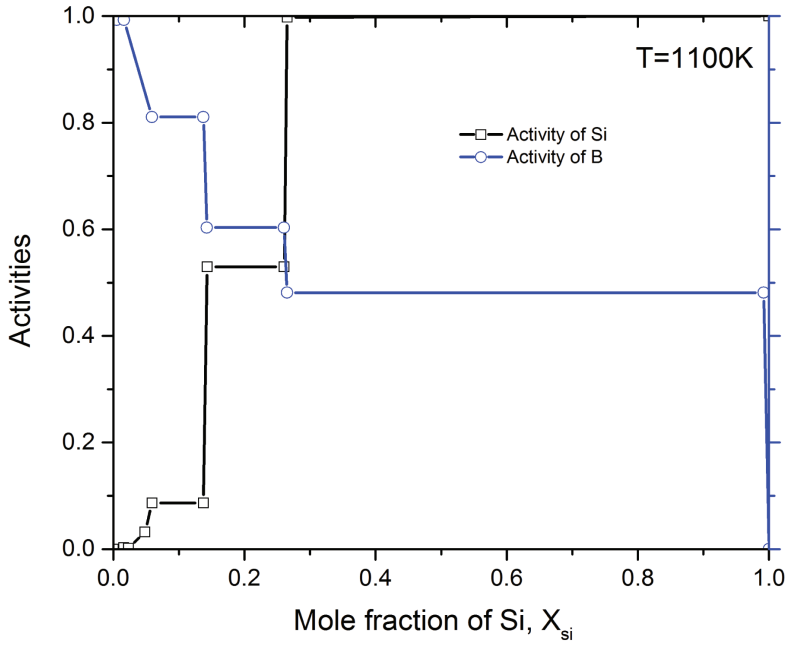


**Figure 4:** Activity of B and Si in a liquid Si melt at 1100 K.

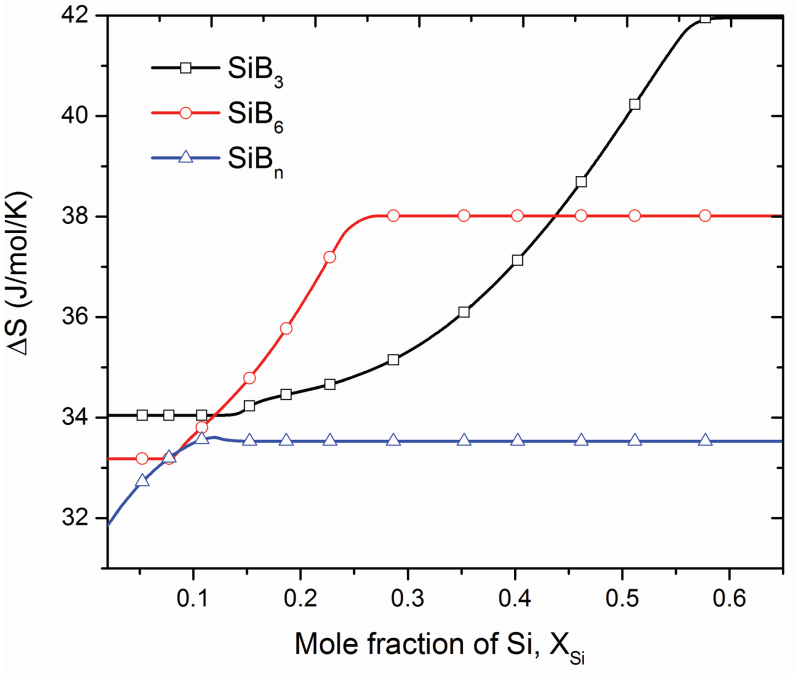


**Figure 5:** The change in entropy (ΔS) with the function of mol % of Si at 1100 K.

1100 K. This indicates the drastic change in Si and B activity level at 1100 K for this phase. In addition, the slope confirms that the $SiB_6$ is not a single line compound. The Si activity increases from 0.0865 to 0.53 in $SiB_6$ phase region, but remains constant (Figure 4) at the two other phase regions: $SiB_n$ + $SiB_6$ or $SiB_6$ + $SiB_3$.

The entropy for this phase is calculated at 1100 K in Figure 5. The highest entropy of the $SiB_6$ phase (~38 J/mol*K) is lower than the highest entropy of the $SiB_3$ phase (~42 J/mol*K). However, the entropy of the $SiB_6$ phase is higher than the $SiB_n$ phase (~32 J/mol*K).

### Silicon n boride ($Sib_n$)

In the boron-rich Si-B system, a compound named $SiB_n$ is introduced where boron content is higher than ~ 94%. Different studies show the existence of $SiB_n$, where n lies between 12 and 50 [42–44]. Both the literature data (Table 2) and the current model (Figures 2 and 3) have outlined the thermodynamic stability of this compound. As presented in Figure 2, the invariant reaction (eq. (5)) for this phase is found at 2310 K, which is consistent with the existing literature [20].

$$Liquid + \beta B \leftrightarrow SiB_n \tag{5}$$

It shows a highly negative Gibbs energy ($\Delta G_f^o = -22.69$ KJ/mol) at 1100 K for the high-boron content region. This indicates a higher stability of this phase in this composition range. The formation of Gibbs energy of this phase at 1800 K, as found in different studies, is presented in Table 2. The activity of Si and B are also calculated at 1100 K for this region, as shown in Figure 4. The activity of Si increases with an increase in mol% of Si in this high-boron content region. The activity of Si increases from 0.001 to 0.086 at 1100 K in this compositional range (mol% of Si 2–6%). The entropy calculated for this phase is the lowest in the boron-rich Si-B system. The highest entropy for this phase is ~ 32.89 J/mol*K at 1100 K. This indicates that the degree of randomness is the lowest in $SiB_n$ system.

Both the Gibbs energy calculation and the literature data indicate that these three phases are thermodynamically stable at a higher temperature range (Table 2 and Figure 3). All the invariant reactions (eq. 3–5) for different phases suggest that the phases are thermally stable at a very high temperature. The activity calculation confirms the formation of these phases and their regions (mol % based) in the phase diagram, an important step to obtain a single or dual phase compound. In addition, the activity calculation shows a non-ideal behavior of the Si-B system. Apart from these, the degree of randomness is predicted from the entropy calculation of these three phases. For high-temperature thermoelectric materials, the lower degree of randomness is required but, on the other hand, makes it more challenging. A lower degree of randomness contributes to lower thermal vibrations, higher phonon scattering at high temperatures, and generates a lower thermal conductivity towards obtaining a higher ZT.

## Thermoelectric properties of Si-B systems

The main three phases in the Si-B system discussed in the previous section are considered as the main candidates for high-temperature thermoelectric materials, particularly due to their relatively high thermal stability. Two other phase regions (such as a mixture of $SiB_6$ and $SiB_n$) are also found in the literature. Among these phases, $SiB_3$ has the lowest Seebeck coefficient, as shown in Figure 6, based on findings from different studies. The $SiB_n$ and $SiB_6$ phases have comparatively higher Seebeck coefficients. The wide range of non-stoichiometric, chemical compositions of $SiB_n$ is the reason for this higher Seebeck coefficient [49]. Figure 6 shows not only the temperature dependence of Seebeck coefficient for different phases/compositions, but also the effect of the processing method. Hot pressing (HP), sintering, plasma melting, arc melting (AM), spark plasma sintering (SPS), and chemical vapor deposition (CVD) for different phases are also presented in Figure 6 in order to compare the effect of the processing methods on the Seebeck coefficient. Among the various methods, SPS is the most effective one in producing a very high Seebeck coefficient. This is due to the fact that SPS process can generate a highly dense stacking fault in the system [45].

This large increment of the Seebeck coefficient results from the phonon-assisted tunneling (hopping) conduction proposed by Wood and Emin [48, 52, 53] for boron-rich borides. According to the hopping conduction mechanism, the Seebeck coefficient depends on two terms (eq. (6)). First is the average entropy change ($\Delta S$) in the system and average vibrational energy ($E_T$) transported with the carrier [53].

$$\alpha = (T\Delta S + E_T)/qT \tag{6}$$

This equation is simply modified when the average energy (E) is associated with the insertion of charge q and its chemical potential $\eta$ [53],

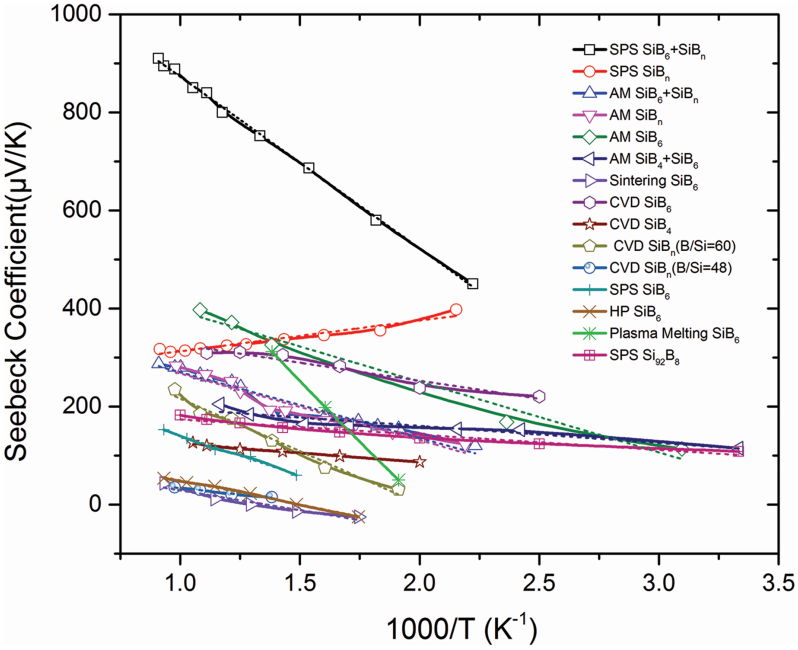


**Figure 6:** Effect of processing method on seebeck coefficient with reciprocal temperature: SPS $SiB_6$ + $SiB_n$ [45], SPS $SiB_n$ [45], AM $SiB_6$ + $SiB_n$ [45], AM $SiB_n$ [45], AM-$SiB_6$ [46], AM- $SiB_4$ + $SiB_6$ [46], Sintering [47], CVD $SiB_6$ [48], CVD $SiB_4$ [48], CVD $SiB_n$(B/Si = 60) [49], CVD $SiB_n$(B/Si = 48), SPS $SiB_6$ [50], HP $SiB_6$ [50], Plasma melting [49], SPS $Si_{92}B_8$ [51].

$$\alpha = (|E - \eta| + E_T)/qT \tag{7}$$

In conventional transport, where low-temperature phonon drag is ignored, only the first term is considered. On the other hand, the second part is contributed if the variable range hopping conduction occurs. In the case of boron or boron-rich borides, the latter part is considered in the literature since it follows the variable range hopping conduction, while the other part remains constant [54]. Figure 6 represents the Seebeck coefficient based on the phonon-assisted hopping conduction (eq. (7)) mechanism for different processing techniques. Average vibration energies ($E_T$) are calculated from the linear curve fitting (R-square > 90) of Figure 6 and summarized in Table 3. As seen from the

**Table 3:** Summary of average vibrational energy, band gap, thermal and mobility activation energy.

| | Average vibrational energy $E_T$ ($\times 10^{-14}$), Joule/mole | Mobility activation energy, $E_a$ ($\times 10^{-20}$), Joule/mole | Band Gap, $E_g$, eV | Thermal Activation Energy, $E_D$ ($\times 10^3$), Joule/mole |
|---|---|---|---|---|
| SPS-$SiB_6$ + $SiB_n$ | 5.61 ± 0.1 | 6.25 ± 0.28 | 0.65 ± 0.03 | 3.19 ± 0.14 |
| SPS-$SiB_n$ | 1.00 ± 0.1 | 0.74 ± 0.02 | 0.025 ± 0.01 | 2.91 ± 0.22 |
| AM-$SiB_6$ + $SiB_n$ | 2.15 ± 0.16 | 3.54 ± 0.26 | 0.33 ± 0.03 | 2.20 ± 0.12 |
| AM-$SiB_n$ | 2.17 ± 0.21 | 0.65 ± 0.02 | 0.04 ± 0.004 | 1.53 ± 0.10 |
| AM $SiB_6$ | 2.3 ± 0.22 | 1.59 ± 0.11 | 0.1 ± 0.01 | 9.78 ± 0.94 |
| AM-$SiB_4$ + $SiB_6$ | 0.55 ± 0.1 | 0.79 ± 0.07 | 0.01 ± 0.002 | 1.62 ± 0.10 |
| Sintering $SiB_6$ | 1.29 ± 0.2 | 6.54 ± 0.73 | 0.67 ± 0.082 | 3.87 ± 0.11 |
| CVD $SiB_6$ | 1.17 ± 0.14 | 1.16 ± 0.05 | 0.056 ± 0.001 | 2.02 ± 0.17 |
| CVD $SiB_4$ | 0.62 ± 0.04 | 0.41 ± 0.01 | 0.04 ± 0.0003 | 1.44 ± 0.17 |
| CVD $SiB_n$(B/Si = 60) | 3.43 ± 0.25 | 2.04 ± 0.14 | 0.15 ± 0.014 | – |
| CVD $SiB_n$(B/Si = 48) | 0.82 ± 0.11 | 4.88 ± 0.16 | 0.5 ± 0.017 | – |
| SPS-$SiB_6$ | 2.59 ± 0.26 | 7.06 ± 0.70 | 0.71 ± 0.08 | – |
| HP-$SiB_6$ | 1.57 ± 0.06 | 7.03 ± 0.06 | 0.71 ± 0.07 | – |
| Plasma melting ($SiB_n$) | 7.91 ± 0.14 | 5.62 ± 0.33 | 0.58 ± 0.04 | – |
| $Si_{92}B_8$ | 0.5 ± 0.05 | 0.19 ± 0.01 | 0.064 ± 0.01 | 1.37 ± 0.12 |

calculated data (Table 3), higher average vibration energy ($E_T$) represents a higher Seebeck coefficient.

The Seebeck coefficient also depends on the microstructure, i.e. grain size and the amount of twin boundaries, of the system [49]. The grain size and twin boundaries are, of course, different in different procedures, causing the differences in the Seebeck coefficient. These grains/twin boundaries from stacking faults provide a potential barrier between the grains and in effect increases the average vibrational carrier energy ($E_T$), thereby increasing the Seebeck coefficient [55].

Yet again, the Seebeck coefficient in the boron-rich Si-B system is mostly positive irrespective of the processing methods. This confirms the p-type semiconducting behavior of the Si-B system. The only exceptions are identified for $SiB_6$ at 573 K. At this temperature or below, $SiB_6$ phase shows only n-type semiconducting behavior for both HP and SPS processes.

Figures 7–9 shows the electronic transport properties of the boron-rich silicon system. The electrical conductivity of boron-rich silicon system is extrapolated here to compare its dependency on various processing methods and phases. Increasing electrical transport property in a particular system exclusively depends on carrier concentration tuning [56–59] and/or band structure engineering [56–58, 60, 61]. As seen in Figure 7, the electrical conductivity increases with an increase in temperature for every processing method. This behavior suggests the degenerated performance of the Si-B system [62] resulting from its semiconductor-like behavior at a high temperature [49]. A high temperature causes small polar ion hopping to produce an Arrhenius type relationship which is a thermally activated conductivity with a temperature dependent prefactor for semiconductor properties [63]. Explicitly,

$$\sigma = CT^{-1}\exp(-E_A/kT) \tag{8}$$

Here, $E_A$ is the mobility activation energy, k is the Boltzmann constant, and T is the absolute temperature. Besides, the generalized temperature dependent Arrhenius type conductivity expression is simply [64],

$$\sigma = \sigma_0 \exp\left(-E_g/2kT\right) \tag{9}$$

where $E_g$ is the band gap. By taking logarithm of each side of eqs. (8) and (9), we obtain

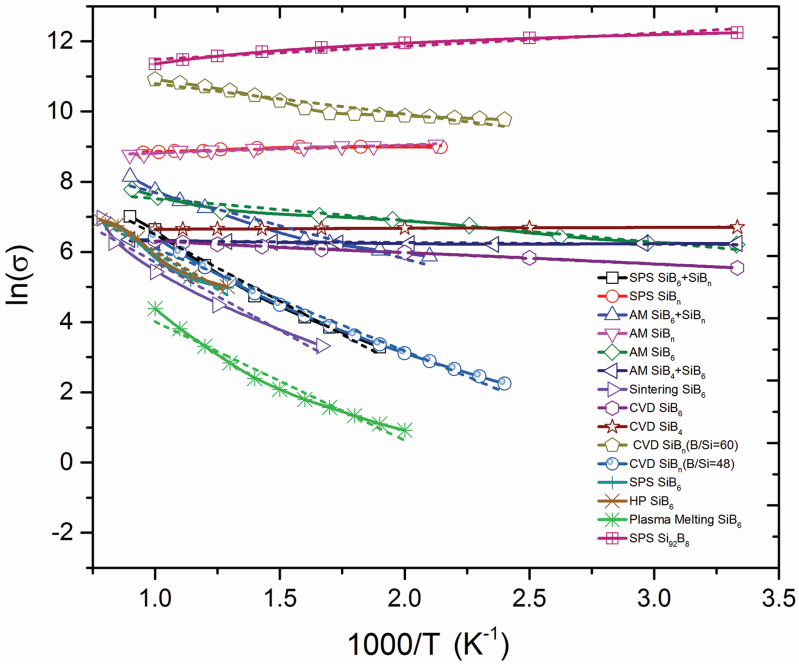


**Figure 7:** A semi log (Arrhenius-type) plot of ln (σ) versus $T^{-1}$: SPS $SiB_6$ + $SiB_n$ [45], SPS $SiB_n$ [45], AM $SiB_6$ + $SiB_n$ [45], AM $SiB_n$ [45], AM-$SiB_6$ [46], AM- $SiB_4$ + $SiB_6$ [46], Sintering [47], CVD $SiB_6$ [48], CVD $SiB_4$ [48], CVD $SiB_n$(B/Si = 60) [49], CVD $SiB_n$(B/Si = 48), SPS $SiB_6$ [50], HP $SiB_6$ [50], Plasma melting [49], SPS $Si_{92}B_8$ [51].

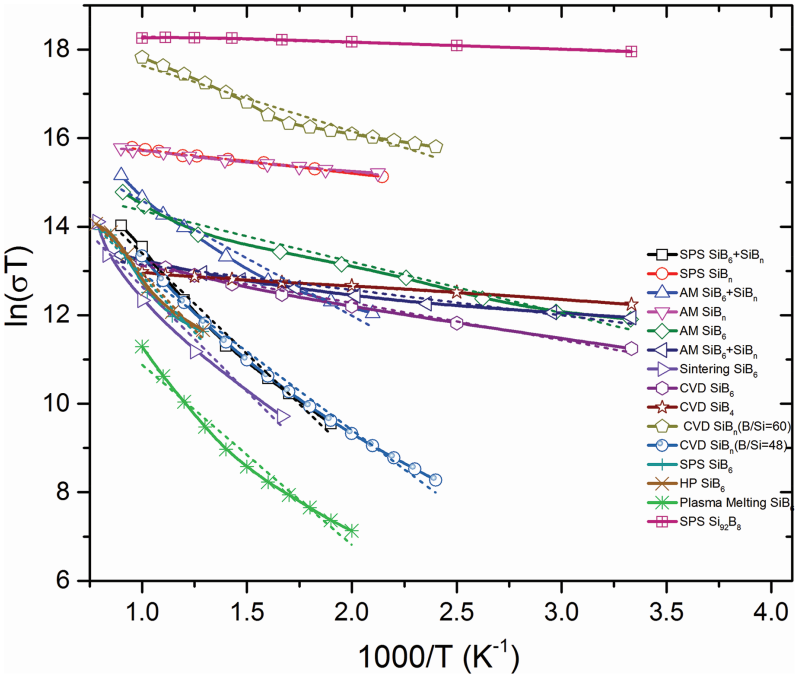


**Figure 8:** A semi log (Arrhenius-type) plot of ln σT versus $T^{-1}$: SPS $SiB_6$ + $SiB_n$ [45], SPS $SiB_n$ [45], AM $SiB_6$ + $SiB_n$ [45], AM $SiB_n$ [45], AM-$SiB_6$ [46], AM- $SiB_4$ + $SiB_6$ [46], Sintering [47], CVD $SiB_6$ [48], CVD $SiB_4$ [48], CVD $SiB_n$(B/Si = 60) [49], CVD $SiB_n$(B/Si = 48), SPS $SiB_6$ [50], HP $SiB_6$ [50], Plasma melting [49], SPS $Si_{92}B_8$ [51].

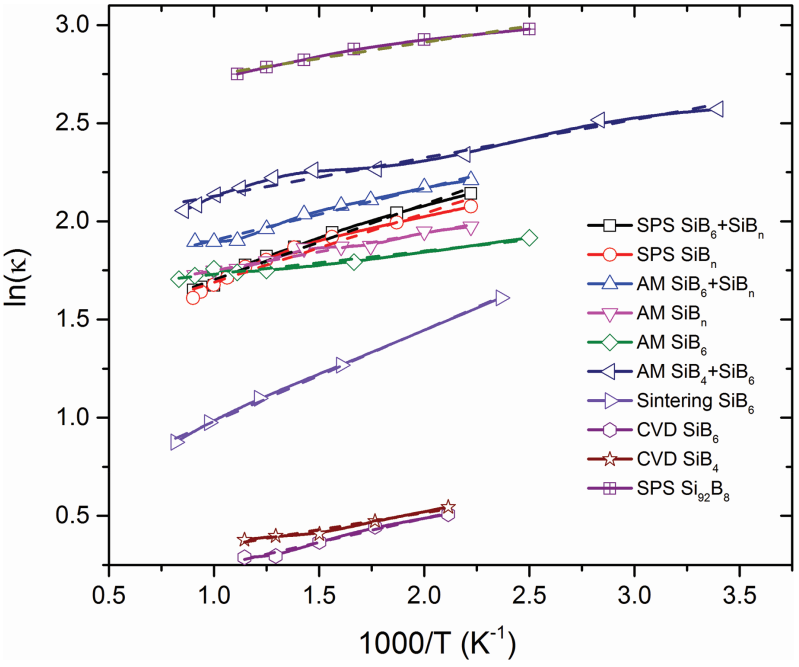


**Figure 9:** A semi-log (Arrhenius-type) plot of ln k versus $T^{-1}$: SPS $SiB_6$ + $SiB_n$ [45], SPS $SiB_n$ [45], AM $SiB_6$ + $SiB_n$ [45], AM $SiB_n$ [45], AM-$SiB_6$ [46], AM- $SiB_4$ + $SiB_6$ [46], Sintering [47], CVD $SiB_6$ [48], CVD $SiB_4$ [48], SPS $Si_{92}B_8$ [51].

$$\ln(\sigma T) = \ln C - \frac{E_A}{k}\frac{1}{T} \tag{10}$$

$$\ln \sigma = \ln \sigma_0 - \frac{E_g}{2k}\frac{1}{T} \tag{11}$$

which indicates that ln (σT) vs. $T^{-1}$ and ln σ vs $T^{-1}$ give a straight line with a slope of $-E_A/k$ and $-E_g/2k$, respectively. Figure 7 and 8 exhibit this linearity (R square > ~94) with the literature data and plotted in an Arrhenius plot. The mobility activation energy ($E_A$) and the band gap ($E_g$) are calculated from this Arrhenius plot and summarized in Table 3.

Both $E_A$ and $E_g$ values correlate with each other. The lower the $E_A$ and $E_g$ values, the higher the conductivity. For example, with an identical processing (SPS) route, $SiB_6$ has higher $E_A$ ($7.06 \times 10^{-20}$ J) and $E_g$ (0.71 eV) values than those of $SiB_n$ ($E_A$ ~ $0.74 \times 10^{-20}$ J, $E_g$ ~ 0.025 eV) phases.

This indicates that the boron content increases the carrier concentration in the valence band which pulls the fermi level down to the conduction band and therefore, the material behaves more like an intrinsic semiconductor. It helps the thermal excitation of electrons from the valence band to conduction band more easily due to the convergence of the band gap, and shows higher conductivity at higher temperatures [56–58, 60, 61]. In addition, the CVD process shows extraordinary electrical conductivity for boron-rich Si-B systems compared to other melting processes. This confirms the fact that the electrical conductivity is affected by melting, which creates microcracks or inner porosity during the solidification [49].

In Figure 9, thermal conductivity is illustrated with respect to temperature for various processing methods. Thermal conductivity decreases with an increase in temperature. Higher amounts of free Si causes a higher thermal conductivity [45, 46, 48, 49, 65]. For example, $Si_{92}B_8$ shows higher thermal conductivity than the other phases. A highly dense system or multiphase system has higher phonon scattering at a higher temperature than a low density system [66–69]. Thermal energy is mainly transmitted through the movement of phonons (lattice thermal diffusion), photons (radiation), and electrons. So, an effective thermal conductivity is represented by the eq. (12) [5, 9],

$$k_{eff} = k_{phonons} + k_{photons} + k_{electrons} \tag{12}$$

The effect of photonic thermal transport within solids is negligible. But the other two components (eq. (12)) are significant towards controlling/reducing the thermal conductivity through the movement of phonons or electronic scattering [5]. It can be depressed by hierarchical architectures [66–69] (atomic/nano/mesostructures, complex phase structures) which provide anharmonic phonon (lattice)/electronic scattering [70].

To understand the thermal conductivity, thermal diffusivity terms (eq. (13)) need to be considered [71].

$$D = \frac{k}{\rho C_p} \tag{13}$$

where D is the thermal diffusivity, ρ is the density and $C_p$ is the specific heat capacity.

Maxwell and Boltzmann's distribution indicates that the thermal diffusion of individual atoms varies over a wide range. And this variation occurs exponentially with a change in the temperature level. Therefore,

$$D = D_0 \exp\left(-\frac{E_D}{RT}\right) \tag{14}$$

$$k = D_0 \rho C_p \exp\left(-\frac{E_D}{RT}\right) \tag{15}$$

where $D_0$ is the pre-exponential factor and $E_D$ is the thermal activation energy for diffusion. By taking logarithm on each side of eq. (15), we obtain

$$lnk = \ln(D_0 \rho C_p) - \frac{E_D}{R} \cdot \frac{1}{T} \tag{16}$$

which indicates that ln (k) vs. $T^{-1}$ gives a straight line with a slope of $-E_D/R$. Figure 9 demonstrates this linearity (R-square > ~92) with the literature data and plotted in a semilog plot (Arrhenius type). The diffusional-thermal activation energy ($E_D$) is calculated from this Arrhenius plot and summarized in Table 3.

From the calculated $E_D$, it can be inferred that the higher the activation energy, the lower the thermal conductivity in different processing routes and phases. This indicates that higher energies are needed when the phonon or the electron scattering occurs due to having different phases, impurities, cracks, grains and grain boundaries. Sintering and SPS exhibit higher diffusional activation energy. In SPS, higher stacking fault with a highly dense system creates the phonon and electron scattering and can obtain a higher activation energy for the SPS process. On the other hand, pores are the main reasons for scattering in the sintering process, and thereby increase the activation energy. The latter process is not suitable for TE materials since these pores are the cause for the low electrical conductivity and Seebeck coefficient.

For a higher ZT, lower thermal conductivity is desired. However, higher density is still preferred due to the resultant high Seebeck coefficient and electrical conductivity, which overcomes the effect of the increased thermal conductivity. Moreover, all of the boron-rich Si-B systems show a decreasing trend of thermal conductivity with an increase in temperature. This advantage makes it a better candidate for high temperature thermoelectric materials.

Figure 10 compares the ZT values found in different studies on the boron-rich silicon borides system. Depending on different processing routes, ZT values differ significantly. The denser the structure, the higher the ZT value of the same phase. The SPS specimen having 90 at.% B ($SiB_6$ + $SiB_n$) shows ZT = ~0.2 in the boron-rich Si-B system [45]. Moreover, arc melted $SiB_n$ shows almost the same ZT at around 1200 K. However, $SiB_6$ via CVD has a lower ZT (~0.01) value at around 1100 K [46]. The Si-rich Si-B system is also discussed in the literature [51]. This phase shows higher ZT (~0.29) than boron-rich borides, as an excess amount of the free Si is present in this system. Though the ZT value is a little higher at 1100 K for Si-rich borides, it has lower thermal stability (Figure 2) than boron-rich borides. All the thermoelectric properties of the boron-rich silicon system are summarized in Table 4.

Figure 11 indicates the dependence of ZT with an increasing boron concentration in the boron-rich borides at a constant temperature. It is observed that $SiB_6$ + $SiB_n$ composite phase shows the maximum ZT at 1100 K. From Figures 10 and 11, it can also be inferred that ZT depends on both boron concentration and the processing routes for B rich borides system. In addition, it can be determined from Figure 5 that ZT also depends on the entropy of the system. Among these three boron-rich Si-B systems, $SiB_n$ shows the lowest degree of randomness. The $SiB_6$ + $SiB_n$ (90 at.% B) composite phase has a higher phonon scattering, since it comprises different phases which give a higher Seebeck coefficient. Due to its lower degree of randomness, phonon/electron scattering and phonon-assisted hopping conduction cause high electrical conductivity and lower thermal conductivity. And this leads to a high ZT of this boron-rich boride system.

Additionally, different studies claim that every material has its peak temperature for ZT [4]. Above that temperature, ZT decreases with an increase in temperature. For example, GeSi is reported to show its peak (ZT = 2) at 1100 K [13], though it can be

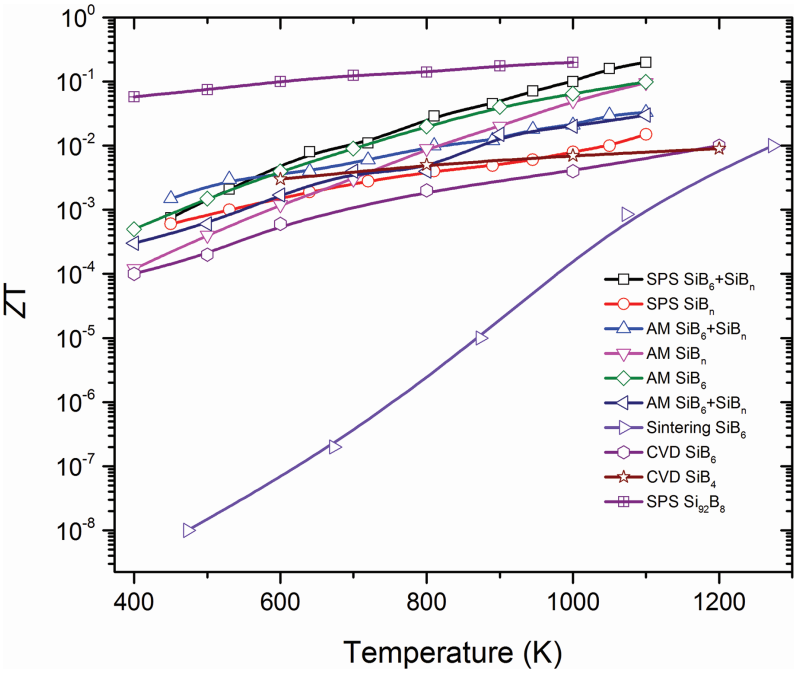


**Figure 10:** Effect of different processing method and temperature on ZT of silicon borides: SPS $SiB_6$ + $SiB_n$ [45], SPS $SiB_n$ [45], AM $SiB_6$ + $SiB_n$ [45], AM $SiB_n$ [45], AM-$SiB_6$ [46], AM- $SiB_4$ + $SiB_6$ [46], Sintering [47], CVD $SiB_6$ [48], CVD $SiB_4$ [48], SPS $Si_{92}B_8$ [51].

**Table 4:** Summary of the thermoelectric properties of Si-B system in the temperature range around 500–1100 K (* different temperature range).

| Phases | Preparation | Seebeck coefficient (μV/K) | Thermal conductivity (W/m*K) | Electrical conductivity (S/m) | Figure of Merit $(ZT)_{max}$ |
|---|---|---|---|---|---|
| $SiB_n$ | SPS [45] | ~397–316 | ~7.96–5.2 | ~8207–7101 | 0.013 |
| | AM [46] | ~135–287 | ~7.18–5.6 | ~7924–6144 | 0.096 |
| | CVD [49] | ~50–250 | – | ~18,233–54,102* (1000 K) | – |
| $SiB_n + SiB_6$ | SPS [45] | ~450–910 | ~8.5–5.2 | ~15–1077 | 0.2 |
| | AM [45] | 120–282 | ~9.11–6.6 | ~315–3196 | 0.04 |
| $SiB_6$ | AM [46] | ~168–453*(1023 K) | ~6.5–5.72 | ~932–2393 | 0.099 |
| | CVD [48] | ~220–309* (900 K) | ~1.70–1.31 | ~377–522 | 0.01 |
| | Sintering [47] | ~ −26–66 | ~5.33–2.62 | ~25–338 | 0.001 |
| $SiB_3$ | CVD [48] AM | ~86–125*(950 K) | ~1.55–1.26 | ~806–750 | 0.008 |
| $SiB_3 + SiB_6$ | [46] | 115–230 | 13.08–7.81 | ~515–573 | 0.03 |

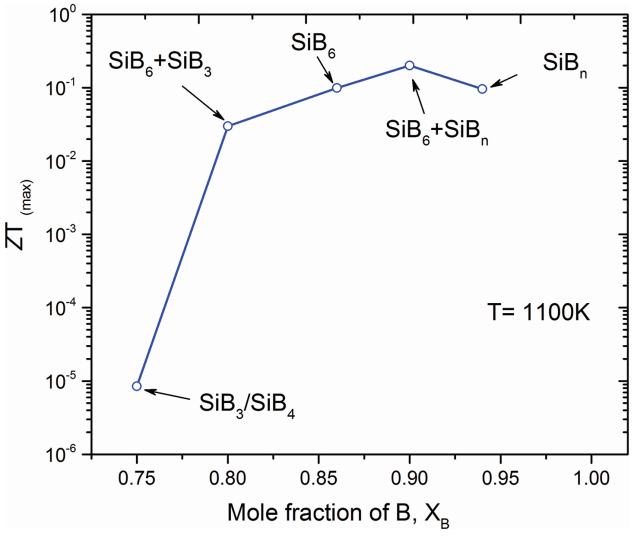


**Figure 11:** Boron content dependence of figure of merit (ZT).

thermally stable up to around 1600 K. The thermoelectric power generation efficiency is higher at that peak temperature. For the boron-rich Si-B system, the peak has not been found in the literature yet. From Figure 10, it is observed that all the ZT values are still on an increasing trend. This observation leads to inspiration for further studies to examine up to 2310 K (melting point of $SiB_n$) to find a super high ZT for an extremely high-temperature condition.

# Conclusion

The boron-rich Si-B system is investigated in this study as a potential high-temperature thermoelectric materials. Both thermodynamic stability and thermoelectric transport properties are reviewed based on the existing literature. Thermodynamic stability of Si-B system is assessed through both the current calculation of Thermo-Calc thermodynamic modeling software and the literature data. The discussion also touches upon other relevant literature on the boron-rich Si-B system. Three single binary phases are identified in the Si-B system. Among these phases, $SiB_n$ and $SiB_6$ show very high melting points of 2310 K and 2122 K, respectively. The high negative formation Gibbs energy of these phases also confirms the thermodynamic stability of the phases. The transport properties, including electrical and thermal conductivity and the Seebeck coefficient of the Si-B system, largely depend on the processing routes and the boron content of the system. This results in a dependence of ZT on those variables. Furthermore, the degree of randomness (entropy) of a system play a vital role on the ZT. In this study, $SiB_n$ exhibits the lowest entropy, and the composite phase ($SiB_6$ + $SiB_n$) that contains $SiB_n$ shows the highest ZT value within the boron-rich Si-B system. In addition, it can be concluded that no peak ZT value has been reported yet for the Si-B system. A further study can be done to investigate the maximum ZT value at extremely high temperatures for the boron-rich silicon borides system.

**Acknowledgements:** The authors gratefully acknowledge the financial support, Grant No. DMR-1310072, of the National Science Foundation (NSF). The authors want to acknowledge the financial support from American Cast Iron Pipe Company (ACIPCO) and Department of Metallurgical and Materials Engineering at the University of Alabama.

## References

[1] EIA, U.S. *International Energy Statistics*. 2016; Available from: https://www.eia.gov/cfapps/ipdbproject/iedindex3.cfm?tid = 44&pid = 44&aid = 2&cid = ww, &syid = 2008&eyid = 2012&unit = QBTU.
[2] BCS, *Waste Heat Recovery: Technology and Opportunities in U.S. Industry*, in *US Department of Energy* 2008.
[3] X. Gou, H. Xiao and S. Yang, Modeling, experimental study and optimization on low-temperature waste heat thermoelectric generator system, Appl. Energy, 87(10) (2010) 3131–3136.
[4] J.-C. Zheng, Recent advances on thermoelectric materials, Front. Phys. China, 3(3) (2008) 269–279.
[5] G.J. Snyder and E.S. Toberer, Complex thermoelectric materials, Nat. Mater., 7(2) (2008) 105–114.
[6] T.J. Seebeck, Magnetische Polarisation der Metalle und Erze durch Temperatur-Differenz, Abhandlungen der Deutschen Akademie der Wissenschaften zu, Berlin (1823), pp. 265–373.
[7] H.J. Goldsmid, Electronic Refrigeration, Pion, London, UK (1986).
[8] G.D. Mahan and J.O. Sofo, The best thermoelectric, Proc. Natl. Acad. Sci. U.S.A., 93(15) (1996) 7436–7439.
[9] R. Eriksson and S. Seetharaman, Thermal diffusivity measurements of some synthetic CaO-Al2O3-SiO2 slags, Metall. Mater. Tran. B, 35(3) (2004) 461–469.
[10] R. Venkatasubramanian, et al., Thin-film thermoelectric devices with high room-temperature figures of merit, Nature, 413(6856) (2001) 597–602.
[11] G. Wu, et al., Properties of sol–Gel derived scratch-resistant nano-porous silica films by a mixed atmosphere treatment, J. Non- Cryst. Solids., 275(3) (2000) 169–174.
[12] G. Joshi, et al., Enhanced Thermoelectric Figure-of-Merit in Nanostructured p-type Silicon Germanium Bulk Alloys, Nano Lett., 8(12) (2008) 4670–4674.
[13] E.K. Lee, et al., Large Thermoelectric Figure-of-Merits from SiGe Nanowires by Simultaneously Measuring Electrical and Thermal Transport Properties, Nano Lett., 12(6) (2012) 2918–2923.
[14] R.W. Olesinski and G.J. Abbaschian, The B–Si (Boron-Silicon) system, Bull. Alloy Phase Digrm., 5(5) (1984) 478–484.
[15] B. Armas, et al., Fabrication and study of electrical properties of boron silicon compounds with high boron concentration, J. Less Common. Met., 47 (1976) 135–140.
[16] Y.O. Esin, et al., Ethalpies formation of liquid alloys of silicon with boron, J. Struct. Prop. Metall. Slag Melts., 3(2) (1978) 182–183.
[17] A. Zaitsev and A. Kodentsov, Thermodynamic properties and phase equilibria in the Si-B system, J. Phase Equilib., 22(2) (2001) 126–135.
[18] A.K. Biletskii, et al., Metals, 3 (1988) 66–68.
[19] R. Noguchi, et al., Thermodynamics of boron in a silicon melt, Metall. Mater. Tran. B, 25(6) (1994) 903–907.
[20] J. Wu, et al., Thermodynamic description of Si-B binary system, Procedia Eng., 31 (2012) 297–301.
[21] A.I. Zaitsev and A.A. Kodentsov, Thermodynamic properties and phase equilibria in the Si-B system, J. Phase Equilib., 22(2) (2001) 126–135.
[22] B. Armas, et al., A study of the thermal decomposition of gaseous Si-B bromides under reduced pressure, J. Less Common. Met., 67(2) (1979) 449–453.
[23] J.-O. Andersson, et al., Thermo-Calc & DICTRA, computational tools for materials science, Calphad, 26(2) (2002) 273–312.
[24] R.W. Cahn, Binary Alloy Phase Diagrams, Adv. Mater., 3(12) (1991) 628–629.
[25] H. Moissan and A. Stock, Preparation and Properties of Two Silicon Borides: $SiB_3$ and $SiB_6$, C. R. Acad. Sci. (Paris), 131 (1900) 139–143.
[26] G.V. Samsonov and V.P. Latysheva, Doklady Akad, Nauk SSSR, 405 (1955) 104–108.
[27] J.R. Salvador, et al., Stabilization of beta-$SiB_3$ from liquid Ga: A boron-rich binary semiconductor resistant to high-temperature air oxidation, Angew Chem., 42(17) (2003) 1929–1932.
[28] C. Brosset and B. Magnusson, The silicon-boron system, Nature, 187 (1960) 54–55.
[29] C.F. Cline and D.E. Sands, A New Silicon Boride, $SiB_4$, Nature, 185 (1960) 456–456.
[30] V. Matkovich, A new form of boron silicide, B4Si, Acta Crystallogr., 13(8) (1960) 679–680.
[31] M. Vlasse, et al., The crystal structure of $SiB_6$, J. Solid State Chem., 63(1) (1986) 31–45.
[32] B. Armas, et al., Determination of the boron-rich side of the B-Si phase diagram, J. Less Common. Met., 82 (1981) 245–254.
[33] L. Kaufman, et al., Coupled pair potential, thermochemical and phase diagram data for transition metal binary systems-VII, Calphad, 8(1) (1984) 25–66.
[34] N.A. Arutyunyan, A.I. Zaitsev and N.G. Shaposhnikov, Analyzing the phase composition of Si-B and Si-B-Ti alloys based on silicon, Russ J. Phys. Chem. A, 86(3) (2012) 339–341.
[35] R.R. Dirkx and K.E. Spear, Optimization of thermodynamic data for silicon borides, Calphad, 11(2) (1987) 167–175.
[36] O.P. Watts, An Investigation of the Borides and the Silicides, Madison, WI: University of Wisconsin (1906).
[37] E. Colton, On the boron-silicon reaction, J. Inorg. Nucl. Chem., 17(1) (1961) 108–111.
[38] L. Brewer, et al., J. Am. Ceram. Soc., 34 (1951) 173–179.
[39] J.A. Stavrolakis, H.N. Barr and H.H. Rice, Investigation of Boride Cermets, J. Am. Ceram. Soc. Bull., 35(2) (1956) 47–52.
[40] C.F. Cline, Preliminary Investigations of the Silicon Boride, $SiB_6$, Nature, 181 (1958) 470–477.
[41] C.F. Cline, An Investigation of the Compound Silicon Boride ($SiB_6$), J. Electrochem. Soc., 106(4) (1959) 322–325.
[42] W. Dietze, M. Miller and E. Amberger, Electron. Technol., 3(1–2) (1970) 73–79.
[43] H. Nowotny, E. Dimakopoulou and H. Kudielka, Untersuchungen in den Dreistoffsystemen: Molybdän-Silizium-Bor, Wolfram-Silizium-Bor und in dem System: $VSi_2$–$TaSi_2$, Monatshefte für Chemie und verwandte Teile anderer Wissenschaften, 88(2) (1957) 180–192.

[44] V. Matkovich, R. Giese and J. Economy, Packing of B12 groups in boron and boride structures, Zeitschrift für Kristallographie-Crystalline Materials, 122(1–6) (1965) 116–130.
[45] L. Chen, et al., Synthesis and thermoelectric properties of boron-rich silicon borides, Mater. Trans. JIM, 37(5) (1996) 1182–1185.
[46] L. Chen, et al. *Microstructure and thermoelectric properties of arc-melted silicon borides*. in *Thermoelectrics, 1997. Proceedings ICT '97. XVI International Conference on*. 1997.
[47] N. Takashima, Y. Azuma and J.-I. Matsushita. *High-Temperature Thermoelectric Properties of Silicon Boride Ceramics as a Smart Material*. in *MRS Proceedings*. 1999. Cambridge Univ Press.
[48] M. Mukaida, T. Goto and T. Hirai, Thermoelectrical Properties of Si-Ti-B In Situ Composite Plates Prepared by Chemical Vapor Deposition, Mater. Manuf. Process, 7(4) (1992) 625–647.
[49] M. Mukaida, et al. *Influence of structures and compositions on thermoelectric properties of silicon borides*. in *Thermoelectrics, 2001. Proceedings ICT 2001. XX International Conference on*. 2001. IEEE.
[50] S.-H. Shim, et al., Thermoelectric characteristics of the spark plasma-sintered silicon boride ceramics, J. Korean Cryst. Growth Cryst. Technol., 15(2) (2005) 75–78.
[51] J. Xie, et al., Thermoelectric properties of Si/$SiB_3$ sub-micro composite prepared by melt-spinning technique, J. Appl. Phys., 118(6) (2015) 065103.
[52] C. Wood and D. Emin, Conduction mechanism in boron carbide, Phys. Rev. B, 29(8) (1984) 4582–4587.
[53] D. Emin, Thermoelectric Power Due to Electronic Hopping Motion, Phys. Rev. Lett., 35(13) (1975) 882–885.
[54] T. Nakayama, J. Shimizu and K. Kimura, Thermoelectric Properties of Metal-Doped β-Rhombohedral Boron, J. Solid State Chem., 154(1) (2000) 13–19.
[55] J. Martin, et al., Enhanced Seebeck coefficient through energy-barrier scattering in PbTe nanocomposites, Phys. Rev. B, 79(11) (2009) 115311.
[56] H. Wang, et al., Heavily Doped p-Type PbSe with High Thermoelectric Performance: An Alternative for PbTe, Adv. Mater., 23(11) (2011) 1366–1370.
[57] H. Wang, et al., Weak electron–Phonon coupling contributing to high thermoelectric performance in n-type PbSe, Proc. Natl. Acad. Sci., 109(25) (2012) 9705–9709.
[58] Y. Pei, et al., Stabilizing the optimal carrier concentration for high thermoelectric efficiency, Adv. Mater., 23(47) (2011) 5674–5678.
[59] L.-D. Zhao, V.P. Dravid and M.G. Kanatzidis, The panoscopic approach to high performance thermoelectrics, Energy Environ. Sci., 7(1) (2014) 251–268.
[60] J.P. Heremans, et al., Enhancement of thermoelectric efficiency in PbTe by distortion of the electronic density of states, Science, 321(5888) (2008) 554–557.
[61] Y. Pei, et al., Convergence of electronic bands for high performance bulk thermoelectrics, Nature, 473(7345) (2011) 66–69.
[62] T. Goto, M.M.a.T.H., Chemical Vapor Deposition of Refractory Metals and Ceramics, Mater. Res. Soc. Symp. Proc., 168 (1990) 159–168.
[63] D. Emin, Small polarons, Phys. Today, 35(6) (1982) 34–40.
[64] J.F. Shackelford, Introduction to Materials Science for Engineers, Pearson Education,Inc (2005).
[65] J. Li, T. Goto and T. Hirai, Thermoelectric Properties of $B_4C$-$SiB_n$ (n = 4,6,14) In-situ Composites, Mater. Trans. JIM, 40(4) (1999) 314–319.
[66] K. Biswas, et al., High-performance bulk thermoelectrics with all-scale hierarchical architectures, Nature, 489(7416) (2012) 414–418.
[67] L. Zhao, et al., All-scale hierarchical thermoelectrics: MgTe in PbTe facilitates valence band convergence and suppresses bipolar thermal transport for high performance, Energy Environ. Sci., 6(11) (2013) 3346–3355.
[68] L.-D. Zhao, et al., High thermoelectric performance via hierarchical compositionally alloyed nanostructures, J. Am. Chem. Soc., 135(19) (2013) 7364–7370.
[69] L.-D. Zhao, et al., Raising the thermoelectric performance of p-type PbS with endotaxial nanostructuring and valence-band offset engineering using CdS and ZnS, J. Am. Chem. Soc., 134 (39) (2012) 16327–16336.
[70] O. Delaire, et al., Giant anharmonic phonon scattering in PbTe, Nat. Mater., 10(8) (2011) 614–619.
[71] J. Unsworth and F.J. Duarte, Heat diffusion in a solid sphere and Fourier theory: An elementary practical example, Am. J. Phys., 47(11) (1979) 981–983.